

Many-body effects at the origin of structural transitions in B_2O_3 ^{EP}

Cite as: J. Chem. Phys. **151**, 224508 (2019); <https://doi.org/10.1063/1.5131763>

Submitted: 15 October 2019 • Accepted: 27 November 2019 • Published Online: 12 December 2019

Axelle Baroni, Fabien Pacaud,  Mathieu Salanne, et al.

COLLECTIONS

 This paper was selected as an Editor's Pick



View Online



Export Citation



CrossMark

ARTICLES YOU MAY BE INTERESTED IN

[Structural study of \$Na_2O-B_2O_3-SiO_2\$ glasses from molecular simulations using a polarizable force field](#)

The Journal of Chemical Physics **147**, 161711 (2017); <https://doi.org/10.1063/1.4992799>

[New interaction potentials for borate glasses with mixed network formers](#)

The Journal of Chemical Physics **152**, 104501 (2020); <https://doi.org/10.1063/1.5142605>

[CP2K: An electronic structure and molecular dynamics software package - Quickstep: Efficient and accurate electronic structure calculations](#)

The Journal of Chemical Physics **152**, 194103 (2020); <https://doi.org/10.1063/5.0007045>



Time to get excited.
Lock-in Amplifiers – from DC to 8.5 GHz

[Find out more](#)

 Zurich
Instruments

Many-body effects at the origin of structural transitions in B_2O_3

Cite as: J. Chem. Phys. 151, 224508 (2019); doi: 10.1063/1.5131763

Submitted: 15 October 2019 • Accepted: 27 November 2019 •

Published Online: 12 December 2019



View Online



Export Citation



CrossMark

Axelle Baroni,^{1,2,3} Fabien Pacaud,^{1,4} Mathieu Salanne,^{1,a)}  Matthieu Micoulaut,²  Jean-Marc Delage,⁴ 
Anita Zeidler,⁵  Philip S. Salmon,⁵  and Guillaume Ferlat^{3,b)} 

AFFILIATIONS

¹Sorbonne Université, CNRS, PHENIX, F-75005 Paris, France

²Sorbonne Université, CNRS, LPTMC, F-75005 Paris, France

³Sorbonne Université, CNRS, MNHN, IRD, IMPMC, F-75005 Paris, France

⁴CEA, DEN, Laboratoire d'Etude des Matériaux et Procédés Actifs, 30207 Bagnols-sur-Cèze, France

⁵Department of Physics, University of Bath, Bath BA2 7AY, United Kingdom

^{a)}Electronic mail: mathieu.salanne@sorbonne-universite.fr

^{b)}Electronic mail: guillaume.ferlat@sorbonne-universite.fr

ABSTRACT

The structural properties of glassy diboron trioxide, g- B_2O_3 , are investigated from ambient to high pressure conditions using two types of atomic force-field models that account for many-body effects. These models are parameterized by a dipole- and force-fitting procedure of reference datasets created via *first-principles* calculations on a series of configurations. The predictions of the models are tested against experimental data, where particular attention is paid to the structural transitions in g- B_2O_3 that involve changes to both the short- and medium-range order. The models outperform those previously devised, where improvement originates from the incorporation of two key physical ingredients, namely, (i) the polarizability of the oxide ion and (ii) the ability of an oxide ion to change both size and shape in response to its coordination environment. The results highlight the importance of many-body effects for accurately modeling this challenging system.

Published under license by AIP Publishing. <https://doi.org/10.1063/1.5131763>

I. INTRODUCTION

Diboron trioxide, B_2O_3 , is an atypical network-forming system that shows, despite its chemical simplicity, a variety of structural motifs in both its crystalline and glassy phases (see Fig. 1 and, e.g., Ref. 1 for a review). Two crystalline polymorphs have so far been reported from experiment. The structure of B_2O_3 -I is based on a network of corner-sharing BO_3 triangular units,² where all of the boron atoms are threefold coordinated (B_3), whereas the structure of B_2O_3 -II is based on a network of corner-sharing BO_4 tetrahedral units,³ where all of the boron atoms are fourfold coordinated (B_4). The crystallization of these polymorphs from the melt requires the application of pressure, typically above 0.4 and 2.0 GPa for the formation of B_2O_3 -I and B_2O_3 -II, respectively.⁴ The crystal structures have mass densities of $\rho \approx 2.56 \text{ g cm}^{-3}$ (B_2O_3 -I) and $\rho \approx 3.11 \text{ g cm}^{-3}$ (B_2O_3 -II). In comparison, the glassy

phase, g- B_2O_3 , has a much smaller density $\rho \approx 1.8 \text{ g cm}^{-3}$ under ambient conditions. Here, the glass structure is dominated by boroxol rings,⁵ which are superstructural units of planar rings constructed from three BO_3 units [Fig. 1(c)]. These rings stabilize low-density boron oxide networks, not only in g- B_2O_3 but also in several predicted crystalline phases⁶⁻⁹ (see Ref. 10 for a review). Thus, rich structural complexity is expected for g- B_2O_3 as the pressure (or density) is changed. This expectation is confirmed by experimental investigations of the pressurized glass. A dissolution of boroxol rings is observed at low density as the rings are broken into a network of BO_3 motifs.¹¹⁻¹³ At higher density, there is a more abrupt transformation into a network of BO_4 motifs.¹²⁻¹⁵ The B_2O_3 system therefore provides an excellent test bed for assessing the key physical ingredients that are necessary to obtain realistic structural models of borate glasses from computer simulations.

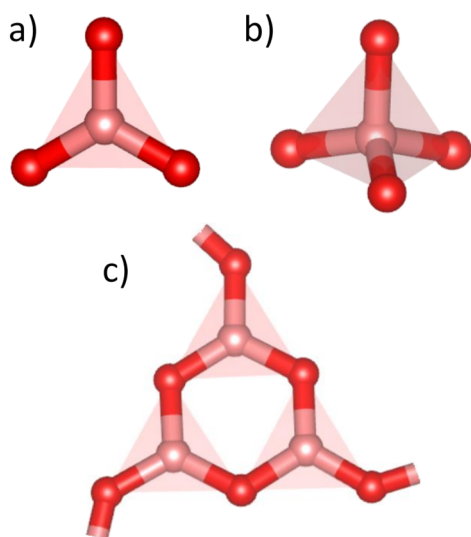


FIG. 1. Structural units found in B_2O_3 network structures, where the B and O atoms are represented by pink and red spheres, respectively. (a) Threefold coordinated boron atom (B_3); (b) fourfold coordinated boron atom (B_4); (c) $B_3O_{9/2}$ boroxol group containing a six-membered B_3O_3 boroxol ring.

In the past, *first-principles* molecular dynamics (FPMD) simulations within the density functional theory (DFT) framework have been used to investigate the structure of liquid and glassy B_2O_3 from ambient to high-pressure conditions.^{5,15–19} However, the affordable system sizes and time scales are limited severely by the computational cost of these simulations. Previous FPMD studies of B_2O_3 have typically been restricted to systems of about 150 atoms and trajectories of a few tens of picoseconds. Unfortunately, such short simulations prevent the structural reorganization that is observed experimentally as the liquid is cooled or as the glass is compressed. Thus, less time demanding simulations based upon empirical force fields are highly desirable as an alternative to FPMD.

The modeling of $g\text{-}B_2O_3$ using empirical force fields^{6,7,13,19–40} was initiated four decades ago,^{20,21} but it has also proved challenging and remains a topical subject.¹⁹ Although the ambient glass structure has been firmly established from experiment, showing that all boron atoms are threefold coordinated with a high proportion of them (~65%–80%) inside boroxol rings,^{41–43} all “quench-from-the-melt” models of the glass obtained from molecular dynamics (MD) simulations suffer from at least one of the following pitfalls: the presence of defects (B_4); a severe underestimation of the proportion of boroxol rings; and/or densities (or bond angles or structure factors) that are inconsistent with experiment. These failures have been attributed to imperfections of the force field and to the use of unrealistic quench rates in the simulations (see Ref. 10 for a review of the merits and weaknesses of the various models). Indeed, both aspects are entangled and are particularly acute in the case of B_2O_3 .

In respect of the force field, it should be sufficiently accurate to be able to predict both (i) the formation of boroxol rings (a

many-body entity) and (ii) the ratio of B_3 to B_4 species present in the glass. Not surprisingly, simulations using potentials restricted to pair interactions fail to produce boroxol-ring containing structures, although these rings are sometimes observed in studies that employ higher-order (three- and up to four-body) interactions.^{24,26,34} Often-times, the many-body terms are incorporated via angular constraints^{19,26,30,31} in order to account for the directionality of the covalent bonds. Another issue is the atomic polarizability.^{13,34,40} It has been suggested that interatomic potentials should include terms accounting for the ring stabilization energy, which is expected from delocalized π -bonding.⁴¹ However, this effect can in principle be captured implicitly through, e.g., polarizable or coordination-dependent force fields.

An assessment of the force-field quality for $g\text{-}B_2O_3$, via simulation of the liquid to glass transformation, is obscured by incomplete equilibration. Experimentally, the fraction of boroxol rings increases rapidly as the liquid is cooled and the glass transition temperature T_g is approached,^{44,45} concomitant with a large increase in the viscosity. The equilibration times approach or even exceed the duration of a simulation, thus hindering to a large extent the structural changes observed experimentally. Because the formation of rings is entropically unfavorable,⁴⁶ it is easier numerically to explore the reverse transformation, i.e., ring dissolution, a strategy that we shall adopt in the following work.

In this paper, we will consider classical force-fields for systems of ions with full formal charges, which are carefully parameterized using the results from DFT calculations on a series of crystal and/or glass configurations. Three force fields are considered that were devised in previous studies that had different goals, aimed at investigating (i) the temperature-induced transformations in the liquid,⁴⁰ (ii) the pressure-induced transformations in the glass,¹³ or (iii) the concentration-induced transformations in binary and ternary systems.⁴⁷ The force fields belong to two different families of ionic interaction models. The first is based on the polarizable ion model (PIM), where polarization effects are included but the ionic radii are fixed. The second is based on the aspherical ion model (AIM), where, in addition to the polarization degrees of freedom, an account of aspherical ion deformation effects is included in the short-range repulsion term. In the present work, we benchmark all three of the force fields within a self-consistent framework and extend the tests that were applied previously. The validity of the models is examined by investigating the microscopic origins of the pressure-induced transformations in $g\text{-}B_2O_3$, namely, boroxol ring dissolution and the transition from B_3 to B_4 species. Additional tests are based on investigations of the crystal structures and the nature of the ambient pressure glass.

The results highlight the ingredients that are required to capture subtle yet important many-body effects that are necessary to model accurately the structure of this challenging system. We also provide new evidence for the energetic origin of boroxol rings.

II. METHODS

A. Interaction potentials

At the simplest level, the pairwise additive models generally used in classical molecular dynamics (MD) simulations reproduce reasonably well the structure of many condensed phase systems. In

oxides, generalized forms of the Born-Huggins-Mayer potential^{48–50} are commonly employed,^{51–53}

$$V_{\text{BHM}} = V_{\text{rep}} + V_{\text{Coul}} + V_{\text{disp}}, \quad (1)$$

where $V_{\text{rep}} = \sum_{i<j} A^{ij} \exp(-a^{ij} r^{ij})$ is a short-range repulsion term,

$V_{\text{Coul}} = \sum_{i<j} \frac{q^i q^j}{r^{ij}}$ describes the Coulomb interactions, and q^i is the

formal charge on ion i . The dispersion term V_{disp} is usually limited to the first two leading terms of the asymptotic multipole expansion,

$$V_{\text{disp}} = - \sum_{i<j} \left[f_6^{ij}(r^{ij}) \frac{C_6^{ij}}{(r^{ij})^6} + f_8^{ij}(r^{ij}) \frac{C_8^{ij}}{(r^{ij})^8} \right],$$

where C_6^{ij} and C_8^{ij} are the dipole-dipole and dipole-quadrupole dispersion coefficients, respectively. A correction for short-range penetration is made using Tang-Toennies damping functions,⁵⁴

$$f_n^{ij}(r^{ij}) = 1 - e^{-b_n^{ij} r^{ij}} \sum_{k=0}^n \frac{(b_n^{ij} r^{ij})^k}{k!}. \quad (2)$$

The resulting simple potentials, in which the interactions depend only on the distance between pairs of ions r^{ij} , are insufficient to model the structure of B_2O_3 . In fact, Madden and co-workers used a series of *ab initio* calculations to show that in many oxide materials it is necessary to take into account many-body effects in order to reproduce the structure as well as other properties of a system such as its vibrational modes.^{55–58} A series of models of increasing complexity were thereby devised to account for these many-body effects.

In the PIM, the response of each ion to the presence of an external field is included by attributing induced dipoles μ^i to each ion i . This leads to an additional polarization component to the interaction potential,

$$V_{\text{pol}} = \sum_{i<j} \left[\frac{q^i \mathbf{r}^{ij} \cdot \mu^j}{(r^{ij})^3} g_D^{ij}(r^{ij}) - \frac{\mu^i \cdot \mathbf{r}^{ij} q^j}{(r^{ij})^3} g_D^{ji}(r^{ij}) + \frac{\mu^i \cdot \mu^j}{(r^{ij})^3} - \frac{3(\mathbf{r}^{ij} \cdot \mu^i)(\mathbf{r}^{ij} \cdot \mu^j)}{(r^{ij})^5} \right] + \sum_i \frac{1}{2\alpha^i} |\mu^i|^2, \quad (3)$$

where the first two terms describe charge-dipole interactions and the last two terms describe dipole-dipole interactions. Tang-Toennies functions⁵⁴ are again used to account for short-range effects in the charge-dipole interaction,

$$g_D^{ij}(r^{ij}) = 1 - c_D^{ij} e^{-b_D^{ij} r^{ij}} \sum_{k=0}^n \frac{(b_D^{ij} r^{ij})^k}{k!}. \quad (4)$$

In Eq. (3), the last term corresponds to the energy cost of deforming the charge density of ion i of polarizability α^i . The induced dipoles are treated as additional degrees of freedom, which have to be determined self-consistently at each step of the simulation. In our case, this is done by minimizing V_{pol} . The induced dipoles depend on the positions of all the atoms such that the polarization term has a many-body essence, despite the pairwise additive form of Eq. (3). The total potential in the PIM is given by

$$V_{\text{PIM}} = V_{\text{BHM}} + V_{\text{pol}}. \quad (5)$$

The AIM is representative of a more sophisticated class of ionic interaction models, in which the repulsion term is no longer represented by a single-variable analytical function such as in the Born-Huggins-Mayer potential. Instead, additional degrees of freedom are attributed to the oxide ion, allowing it to *breathe* in an aspherical way, in response to its changing nearest-neighbor environment.^{59–61} In practice, the interparticle distance in the pair-potential is replaced by the variable quantity,

$$\rho^{ij} = r^{ij} - \delta\sigma^i - \delta\sigma^j - \mathbb{S}_\alpha^{(1)}(v_\alpha^i - v_\alpha^j) - \mathbb{S}_{\alpha\beta}^{(2)}(\kappa_{\alpha\beta}^i + \kappa_{\alpha\beta}^j). \quad (6)$$

The scalar $\delta\sigma^i$ represents the deviation of the radius of the ion from its default value, while v^i and κ^i are sets of three and five variables that describe the dipolar and quadrupolar shape distortion, respectively. $\mathbb{S}^{(1)}$ and $\mathbb{S}^{(2)}$ are the corresponding interaction tensors,

$$\mathbb{S}_\alpha^{(1)} = \frac{r_\alpha^{ij}}{r^{ij}} \quad (7)$$

$$\mathbb{S}_{\alpha\beta}^{(2)} = \frac{3r_\alpha^{ij} r_\beta^{ij}}{r^{ij2}} - \delta_{\alpha\beta}, \quad (8)$$

and $\delta_{\alpha\beta}$ is the Kronecker delta.

In the case of pure B_2O_3 , the resulting repulsion potential is given by

$$V_{\text{asph}} = \sum_{i \in \text{B}, j \in \text{O}} [A^{+-} \exp(-a^{+-} \rho^{ij}) + B^{+-} \exp(-b^{+-} \rho^{ij})] + \sum_{i \in \text{O}, j \in \text{O}, i < j} A^{--} \exp(-a^{--} \rho^{ij}) + \sum_{i \in \text{B}, j \in \text{B}, i < j} A^{++} \exp(-a^{++} \rho^{ij}) + \sum_{i \in \text{O}} \{D[\exp(\beta\delta\sigma^i) + \exp(-\beta\delta\sigma^i)] + [\exp(\zeta^2 |v^i|^2) - 1] + [\exp(\eta^2 |\kappa^i|^2) - 1]\}, \quad (9)$$

where

$$|\kappa^i|^2 = \kappa_{xx}^i{}^2 + \kappa_{yy}^i{}^2 + \kappa_{zz}^i{}^2 + 2(\kappa_{xy}^i{}^2 + \kappa_{xz}^i{}^2 + \kappa_{yz}^i{}^2) \quad (10)$$

and the total AIM potential is given by

$$V_{\text{AIM}} = V_{\text{asph}} + V_{\text{Coul}} + V_{\text{disp}} + V_{\text{pol}}. \quad (11)$$

It is worth noting that no quadrupolar terms were included in V_{pol} because they did not improve the accuracy of the force field (as measured through the fitting procedure described below), and because they often lead to reduced stability of simulations at high temperatures (frequent “polarization catastrophes,” i.e., numerical instabilities leading to nonphysical overpolarization, may occur⁶²).

B. Parameterization from DFT calculations

The atomic or pairwise additive parameters in the PIM and AIM all have a well-defined physical origin, and a methodology has been set-up to determine them from DFT calculations alone.^{63,64} The procedure is as follows:⁶⁵

1. Generate a number N_c of typical condensed-phase configurations.
2. Perform DFT calculations on each of these configurations to:
 - (a) Determine the ground-state wavefunctions, which give access to the *first-principles* force components \mathbf{F}_{DFT} .
 - (b) Find the localized Wannier functions, from which the *first-principles* induced dipole components $\boldsymbol{\mu}_{\text{DFT}}$ are calculated.
3. Minimize the function χ_D^2 with respect to the parameters of the polarization term (V_{pol}), where

$$\chi_D^2 = \frac{1}{N_c} \sum_{j=1}^{N_c} \frac{1}{N_j} \sum_{i=1}^{N_j} \frac{|\boldsymbol{\mu}_{\text{DFT}}^i - \boldsymbol{\mu}_{\text{PIM/AIM}}^i|^2}{|\boldsymbol{\mu}_{\text{DFT}}^i|^2} \quad (12)$$

and N_j is the number of atoms in configuration j .

4. Minimize the function χ_F^2 with respect to the parameters of the repulsion term (V_{BHM} for the PIM or V_{asph} for the AIM), where

$$\chi_F^2 = \frac{1}{N_c} \sum_{j=1}^{N_c} \frac{1}{N_j} \sum_{i=1}^{N_j} \frac{|\mathbf{F}_{\text{DFT}}^i - \mathbf{F}_{\text{PIM/AIM}}^i|^2}{|\mathbf{F}_{\text{DFT}}^i|^2}. \quad (13)$$

In the case of B_2O_3 , the reference DFT calculations were performed using the Perdew-Burke-Ernzerhof (PBE) generalized gradient approximation (GGA) for the exchange-correlation energy.⁶⁶ First, we determined the parameters of the AIM by combining dipole-fitting and force-fitting for a set of four configurations that included the crystalline polymorphs B_2O_3 -I ($\rho = 2.56 \text{ g cm}^{-3}$) and B_2O_3 -II ($\rho = 3.11 \text{ g cm}^{-3}$), and two structures of glassy B_2O_3 generated⁶⁷ for the ambient conditions, density $\rho = 1.84 \text{ g cm}^{-3}$. Note that only the B_2O_3 -II configuration contained fourfold coordinated boron atoms. The χ_D^2 and χ_F^2 values were 0.027 and 0.263, respectively, which indicate good overall reproduction of the DFT reference data.⁶⁵ (The different orders of magnitude for χ_D^2 vs χ_F^2 reflect mostly the fact that the dipoles have a finite average value, whereas the magnitude of the forces is centered around zero. The latter can lead to large differences for small force values.) In an attempt to fit the parameters of the PIM to the same set of configurations, the difference with DFT gets much larger and some parameters take unphysical values due to large error compensations. However, by restricting

the fit to the two glassy configurations alone, we could get a better-behaved PIM potential, denoted by PIM-Fit 1 in the following. In order to gain a measure of the transferability of this potential with respect to the AIM, χ_D^2 and χ_F^2 were also calculated for the same set of four configurations: values of 0.031 and 0.499 were obtained, respectively.

Finally, a second PIM potential was fitted using a different and larger set of 36 configurations, chosen from seven different compositions of borosilicates, including sodium- and lithium-containing glasses. In these systems, the ratio of B_3 to B_4 species can be tuned by changing the alkali to boron oxide ratio. The derived model, denoted by PIM-Fit 2, has been used recently for the study of $\text{Na}_2\text{O}-\text{B}_2\text{O}_3-\text{SiO}_2$ glasses.⁴⁷ In its application to pure B_2O_3 , the model delivers poorer performance ($\chi_D^2 = 0.030$ and $\chi_F^2 = 0.890$). However, we use it in order to make a comparative assessment of the high-pressure trends.

The dispersion parameters are the only terms that are not determined from this fitting procedure. Indeed, the dispersion interaction is not accounted for well in standard GGA DFT functionals.⁶⁸⁻⁷⁰ In consequence, this term was added afterwards. Here, the O-O dispersion term was taken from the work of Jahn *et al.*,⁶¹ but no dispersion terms were included for interactions involving the boron atom because of its small polarizability. Values for all of the parameters used in the AIM, PIM-Fit 1, and PIM-Fit 2 potentials are reported in Tables I–III in the Appendix.

In order to analyze further the error associated with each of the models in respect to the DFT calculations, we calculated the parameter $\chi_{F_i}^2$ for each atom i of each configuration. The results are given in Fig. 2 and show that the large average error of the two PIM potentials arises mostly from a few atomic positions for which the error is very large ($\chi_{F_i}^2 > 1$, sometimes reaching 10 for PIM-Fit 2). This contrasts with the AIM potential, for which the errors are smaller and distributed uniformly, with only a few atomic positions for which $\chi_{F_i}^2 \approx 1$. The latter correspond mostly to atoms for which the DFT force is very small, which leads to a large relative error.

C. Simulations

The PIM-Fit 1, PIM-Fit 2, and AIM potentials were tested using structural optimizations of the known crystals and MD

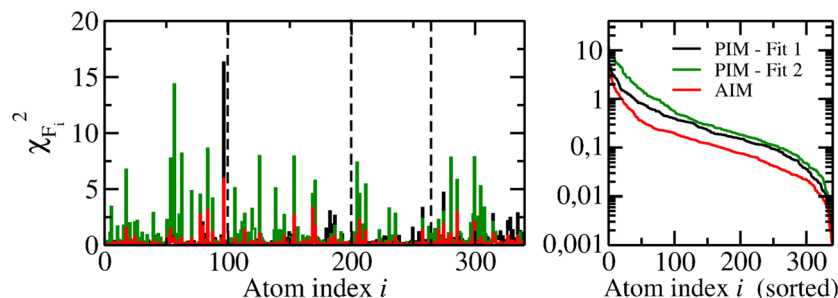


FIG. 2. Estimation of the error made by the empirical interaction potentials in determining the force on each atom relative to the force given by the reference DFT calculations. Left: Each block of data separated by vertical dashed lines corresponds to one of four different configurations, where the first two configurations correspond to glassy systems of 100 atoms, and the second two configurations correspond to orthorhombic supercells for crystalline B_2O_3 -I and B_2O_3 -II. Right: The datasets sorted by decreasing value of $\chi_{F_i}^2$.

simulations of the glass. Part of the high-pressure investigation using the AIM potential is reported in Ref. 13. For the glass, the initial configuration used for the MD simulations was the boroxol-ring rich (320 atom) model obtained in Ref. 5, which gives a density and structure at ambient conditions that are fully consistent with experiments.

A time step of 1 fs was used for all the simulations, and the Coulomb and polarization forces were calculated using the Ewald summation method.^{63,71} Short runs (a few tens of picoseconds) in the *NPT* ensemble were performed at several target pressures. From the configurations obtained, simulations in the *NVT* ensemble were performed for at least 1 ns. The pressures indicated throughout this paper are the average values obtained from the *NVT* (i.e., constant density) runs. All of the potentials used in this study reproduce very well the measured pressure dependence of the density over the entire pressure range of 0–9 GPa probed in the *in situ* experiments of Brazhkin *et al.*¹⁵ (see Fig. 1 of Ref. 13 for the AIM case).

III. RESULTS

A. The B₃ to B₄ transition

Capturing the B₃ to B₄ transition is a challenge for empirical potentials. For example, in the studies of borosilicates and related systems, where the transition is driven by compositional change, Kieu *et al.*⁷² had to adapt the force-field parameters for each composition in order to reproduce the measured speciation. In pure g-B₂O₃, even coordination-dependent potentials^{39,73} have so far failed to reproduce the pressure threshold at which B₄ species start to form¹³ (see below).

We first tested our PIM and AIM potentials using the polymorphs B₂O₃-I and B₂O₃-II that contain solely B₃ and B₄ species, respectively. The dependence of the energy E on volume V was determined at 0 K by changing isotropically the volume of the cell and optimizing the geometry of the systems. The results are shown in Fig. 3. From these plots, one can in principle extract (i) the equilibrium volume of both crystals and (ii) the transition pressure at zero temperature [given by minus the gradient of the common tangent to the two $E(V)$ curves].⁷⁴ While it is clear that all three of the potentials yield similar $E(V)$ relationships for the B₂O₃-I crystal, marked differences are observed for the B₂O₃-II crystal. First, the PIM-Fit 1 potential is unable to stabilize the B₂O₃-II structure, i.e., an equilibrium configuration could not be obtained. This feature reflects the fact that the potential was fitted using configurations with B₃ units alone, i.e., the parameters are unrepresentative of the interactions involving B₄ (tetrahedral) units. In contrast, the PIM-Fit 2 potential overstabilizes B₂O₃-II: it has a lower energy than B₂O₃-I, implying that the latter would be stable only at negative pressure. This feature reflects a tendency to overstabilize B₄ relative to B₃ units. By contrast, the AIM gives the only potential for which the $E(V)$ plots are consistent with both DFT and experiments: while it underestimates the equilibrium volume of both crystals by 3%, which is comparable to the accuracy of the DFT calculations, the predicted transition pressure is 1.7 GPa, in good agreement with DFT (~3 GPa)⁷⁵ and experiments (~2 GPa).⁷⁶

We now turn to the pressure-induced B₃ to B₄ transition in the glass. As a first test of the quality of the potentials, the neutron structure factor $S_N(Q)$ was computed from the MD configurations

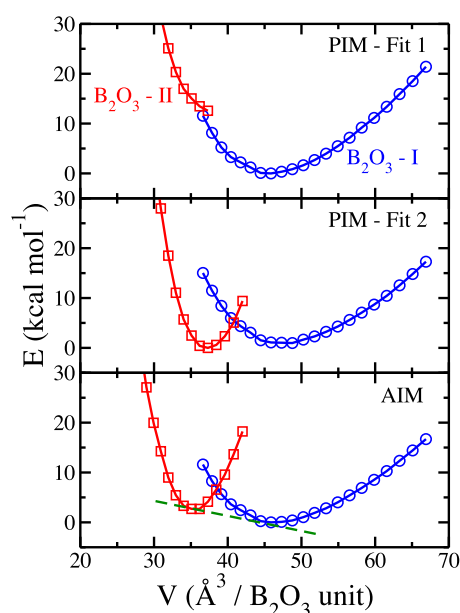


FIG. 3. Volume dependence of the energy for the crystalline structures of B₂O₃-I and B₂O₃-II at 0 K from the PIM-Fit 1, PIM-Fit 2, and AIM potentials. The dashed (green) line is the common tangent to the equilibrium curves.

(see Ref. 13 for details), where Q denotes the magnitude of the scattering vector. The results are compared to the measured neutron diffraction data in Fig. 4. Datasets are reported for three different densities, which correspond experimentally to ambient pressure ($\rho = 1.8 \text{ g cm}^{-3}$), a high-pressure state before the appearance of B₄ units ($\rho = 2.4 \text{ g cm}^{-3}$), and a high-pressure state for which half of the B₃ units have been converted into B₄ tetrahedra ($\rho = 2.7 \text{ g cm}^{-3}$). For each condition, the PIM-Fit 1 and AIM potentials yield

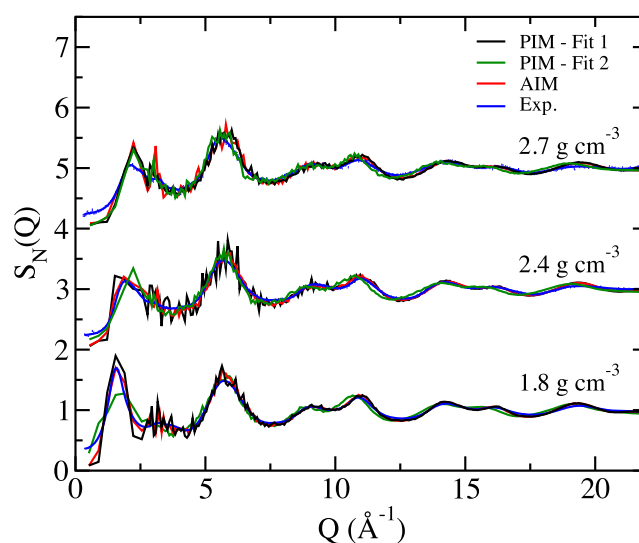


FIG. 4. Neutron total structure factors $S_N(Q)$ for g-B₂O₃ at three different densities. The experimental data are from Ref. 13.

structure factors in good agreement with experiment. In comparison, the PIM-Fit 2 potential leads to discrepancies with experiment that are particularly marked at the lowest density: the intensity of the first peak in $S_N(Q)$ is too low (reflecting an incorrect reproduction of the medium-range order) and there is a small mismatch in phase at larger Q values. The agreement with experiment tends to improve, however, at higher glass density.

A more stringent test of the potentials is provided by comparing the predicted pressure dependence of the boron-oxygen coordination number, \bar{n}_B^O , with the results obtained from different experimental techniques, namely, neutron diffraction,¹³ X-ray diffraction,¹⁵ and inelastic X-ray scattering.¹⁴ As shown in Fig. 5, the potentials yield very different trends at pressures above 3 GPa. It is clear that the PIM-Fit 1 potential is unable to reproduce the B_3 to B_4 transition within the relevant pressure range. This failure is reminiscent of that obtained from all former classical force-fields in the literature.^{39,73} In contrast, the PIM-Fit 2 and AIM potentials show an unprecedented improvement, with values compatible with experiments at pressures up to 10 GPa, and falling in between the experimental and DFT-based MD results¹⁵ above 10 GPa. In the case of the PIM-Fit 2 potential, however, the threshold for the transition pressure is seemingly too low, in line with the pitfalls already evidenced in the crystalline tests, namely, over-stabilization of B_4 units.

Thus, it can be concluded from these first tests that PIM-Fit 1 provides a reasonable model for low-density conditions but fails for high-density conditions, while the situation is reversed for PIM-Fit 2. The AIM provides the only transferable potential over the whole pressure range.

In order to understand this observation, we analyzed in further detail the structural changes that occur during the B_3 - B_4 transition. Figure 6 shows the first peak of the boron-oxygen partial pair-distribution function, $g_{BO}(r)$, for the AIM potential at various densities. Up to a density of 2.4 g cm^{-3} , i.e., before the formation of B_4 units, the peak shape is essentially the same (the decrease of intensity results from a renormalization effect as the density increases). At larger densities (red curves in Fig. 6), a broad shoulder appears at 1.45 – 1.65 \AA , showing the entrance of a fourth oxygen atom into the

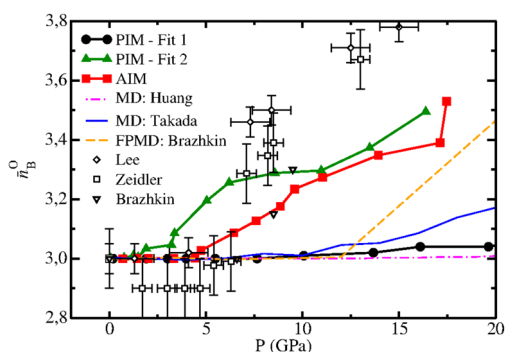


FIG. 5. Pressure dependence of the mean B–O coordination number \bar{n}_B^O in $g\text{-B}_2\text{O}_3$ at ambient temperature predicted by the PIM-Fit 1, PIM-Fit 2, and AIM potentials. The experimental results (open symbols) are from Refs. 13–15. The other MD results are from FPMD [dashed (orange) curve¹⁵] or from empirical force-field models [chained (purple) curve³⁹ and solid (blue) curve⁷³].

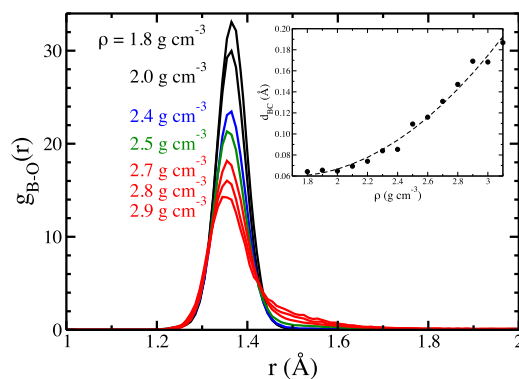


FIG. 6. Density dependence of the first peak in the B–O partial pair-distribution function $g_{BO}(r)$ for $g\text{-B}_2\text{O}_3$ obtained for the AIM potential. Inset: Density dependence of the mean distance between a boron atom B and center C of the plane formed by its three oxygen neighbors in a BO_3 unit.

first coordination shell. This finding points to the pressure-induced formation of asymmetrical B_4 units, in keeping with the observations made in neutron diffraction experiments.¹³ Distorted B_4 units are also found in crystalline $\text{B}_2\text{O}_3\text{-II}$, where the B–O bond lengths vary between 1.37 and 1.51 \AA .³ In comparison, the tetrahedral units are symmetrical in glassy silica and germania at ambient conditions, and there is only one Si–O distance for α -quartz (1.62 \AA).⁷⁷ Another interesting effect of densification is the progressive deformation of planarity of the BO_3 units. As shown first by DFT-based MD,¹⁷ and later confirmed by *in situ* nuclear magnetic resonance (NMR) experiments,⁷⁸ the transition state between B_3 and B_4 is characterized by a small deviation of the boron atom from the center (C) of the plane formed by its three oxygen neighbors. The AIM captures well this behavior, as shown by the variation with the density of the average B–C distance d_{BC} (inset of Fig. 6).

Such complex structural changes are hard to capture by simpler force fields, pointing to a possible reason for the failure of previous simulations to reproduce the B_3 to B_4 transition within the correct pressure range. Indeed, important ingredients of the AIM are the oxide ion breathing and deformation effects, which are included in the short-range repulsion term. In order to investigate further the impact of these effects, we calculated the pairwise repulsion forces between all nearest-neighbor B–O pairs in several configurations. Note that this is easily done despite the many-body nature of the AIM potential, because the ground-state values for all degrees of freedom were accumulated at each time step.

The results are shown in Fig. 7 for two configurations of $g\text{-B}_2\text{O}_3$, with densities of 1.8 g cm^{-3} and 2.9 g cm^{-3} , and for the two crystalline polymorphs. The solid lines show the BHM component V_{BHM} of the potentials corresponding to PIM-Fit 1 and PIM-Fit 2. We see immediately that the BHM components handle well the interaction for B–O pairs either at smaller distances (PIM-Fit 1) or at larger distances in the range of 1.4 – 1.6 \AA , where the fourth oxygen ion is located (PIM-Fit 2), but neither of them is accurate over the entire range of distances. In the AIM, the fourth oxide ion is accommodated into the boron first-neighbor shell through a reduction in the effective radii of the oxide ions. Empirically, if the coordination polyhedra are assumed to be regular polyhedra with touching oxygen atoms, then the measured change in the

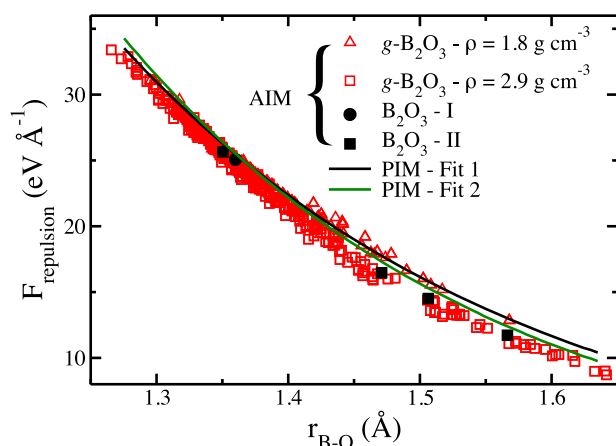


FIG. 7. Dependence of the repulsive force between all B–O first-neighbor pairs on the B–O distance r_{BO} . The datasets correspond to single configurations of $g\text{-B}_2\text{O}_3$ at two different densities and to the crystalline polymorphs $\text{B}_2\text{O}_3\text{-I}$ and $\text{B}_2\text{O}_3\text{-II}$. The solid curves show the BHM component V_{BHM} of the potentials corresponding to PIM-Fit 1 and PIM-Fit 2.

B–O bond length in $g\text{-B}_2\text{O}_3$ from 1.35 Å at ambient pressure (B_3) to 1.42 Å at 17.5 GPa (B_4)¹³ gives a reduction of ≈ 0.01 Å in the oxygen radius.⁷⁹

We note that some potentials should be able to capture these effects by fitting effectively all possible coordination environments (the family of *reactive force-fields*),⁸⁰ although we are not aware of any attempt to model B_2O_3 within such a scheme. In the present work, the breathing and deformation effects mark the response of the ions to their changing environment, which does not need further parameterization. This feature shows that the AIM contains the correct physical ingredients for modeling B_2O_3 .

B. Boroxol rings in the glass

As discussed in Sec. I, boroxol rings are a key feature in the structure of $g\text{-B}_2\text{O}_3$, and their prevalence is commonly enumerated in terms of the proportion f of boron atoms involved in boroxol rings. At ambient conditions, f is in the range of 65%–80%.^{41–43} Quantitative accounts of the pressure dependence of f are scarce,^{12,81,82} but consistently show a reduction of f with increasing pressure, as expected from the ring's low compactness. The pressure at which boroxol rings fully disappear ($f = 0$) is reported to be around 11–14 GPa,^{11,83} corresponding to a density of 2.8–3.0 g cm^{-3} . Figure 8 compares the predictions of the models⁸⁴ with the measured trend. The failure of PIM-Fit 2 is patently obvious and accompanies its poor description of the structure factor $S_N(Q)$ at low density (Fig. 4). The repulsive part of this potential is too strong, which impedes the stabilization of planar six-membered rings. The other two potentials provide the correct trend and are in good agreement with the available experiments, although some caution is required in making this comparison. The experimental results were obtained from *ex situ* experiments for which the effects of structural relaxation are unknown. The glasses were obtained either by quenching from the melt under pressure^{12,81} or by pressure-compaction at a temperature below T_g ,⁸² and were then recovered to ambient conditions where the measurements were made.

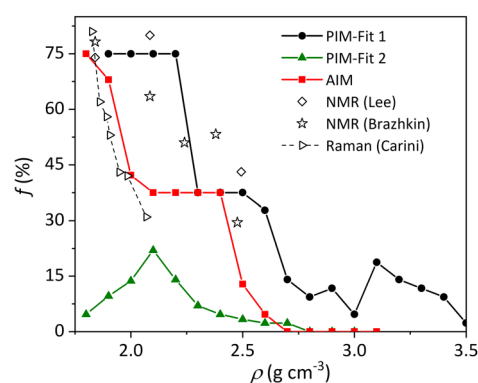


FIG. 8. The density dependence of the proportion of boron atoms in boroxol rings, f , in $g\text{-B}_2\text{O}_3$. The experimental data^{12,81,82} correspond to *ex situ* experiments and were obtained either from quench-from-the-melt (under pressure)^{12,81} or from pressure-compacted (at a temperature below T_g)⁸² glasses. The pressures used to compress the samples^{12,81,82} were converted into densities using Fig. 1 of Ref. 13. The Raman experiments⁸² probe the proportion of oxygen atoms in boroxol rings, f_O , which is here converted⁸⁵ to the proportion of boron atoms in boroxol rings using $f = f_O \times 1.5$.

Finally, we investigated the physical origin of the boroxol ring stability. This issue has been addressed in the past by Maranas *et al.*,³⁴ who pinpointed the polarization term in their potential as leading to an energy for boroxol rings that is slightly lower with respect to nonring units. Here, we determine the boroxol-ring stabilization energy (BSE) for a given potential in the following way. First, we computed the energy (at 0 K) for a large set of glassy configurations with different proportions of boroxol rings ranging from $f = 0$ –75% (all energies were acquired at fixed density, 1.84 g cm^{-3}). Second, we plotted the energies obtained as a function of f and found a linear anticorrelation: the more rings in a given configuration the lower its energy (see Fig. 1 of Ref. 5, for example). Third, we extract the BSE from the slope of this graph. We obtained BSE values of -11.4 kcal (mol boroxol)⁻¹ and -5.8 kcal (mol boroxol)⁻¹ for the PIM-Fit 1 and AIM potentials, respectively.⁸⁶ These values encompass reasonably well the experimental estimate of -6.4 kcal (mol boroxol)⁻¹, indirectly derived from Raman measurements.⁴⁴

To gain further evidence on the crucial role of polarization, we performed “numerical experiments”, in which the oxide ion polarizability α_O is varied, keeping all of the other parameters constant. The BSE was then determined for each of the modified force-fields. Figure 9 shows the evolution of the BSE with α_O for the AIM potential. The larger the polarizability, the smaller the BSE, i.e., the greater the stability of the boroxol rings. When the polarization is turned off ($\alpha_O = 0$), the presence of boroxol rings increases the system energy by 51.4 kcal (mol boroxol)⁻¹: running a simulation of a glass would rapidly lead to the destruction of the initial rings. As the magnitude of the polarizability is increased, the ring stability sets in for $\alpha_O \geq 1.1$ Å³. A similar trend is observed for a similar change of α_O for the PIM potentials. We recently exploited this relationship between the BSE and the polarizability in a study of the liquid-glass transformation:⁴⁰ by artificially increasing α_O in the PIM-Fit 1 potential to compensate for the limited MD equilibration time,

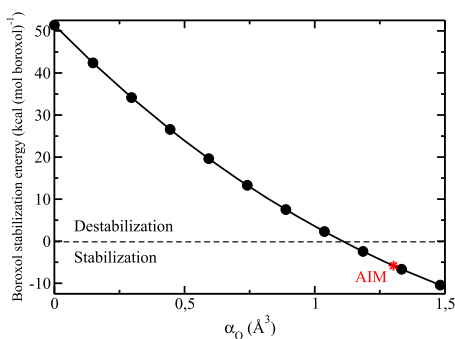


FIG. 9. Variation of the boroxol ring stabilization energy with the polarizability of the oxide ion as calculated within the framework of the AIM. The red asterisk indicates the AIM polarizability as obtained originally from fitting the DFT data.

low temperature structures with large amounts of boroxol rings were obtained.

We conclude that polarizability, an implicit many-body effect, is an essential physical ingredient in any potential aimed at reproducing the formation of boroxol rings, and thus the intermediate-range structure in $g\text{-B}_2\text{O}_3$.

IV. CONCLUSION

We have shown that the intriguing structural features of B_2O_3 result from a subtle balance between the various interionic interactions. In particular, the quality and transferability of the potentials that we have derived is ascribed to the inclusion of crucial many-body characteristics, namely, (i) the ability for an oxide ion to

“breathe” and deform, an important feature for accurately reproducing the B_3 to B_4 transition under pressure, and (ii) the polarizability of the oxide ion, which is at the origin of the boroxol ring stability.

Our AIM potential delivers almost the same accuracy as state-of-the-art DFT but at a fraction of its computational cost. It therefore represents a significant step forward for investigating various structural problems. In particular, when used in conjunction with *enhanced sampling* techniques,⁸⁷ it could allow for an accurate exploration of the relatively unknown B_2O_3 phase-diagram and/or the approach of the liquid to the glass transition.

ACKNOWLEDGMENTS

This work was supported by French state funds managed by the French National Research Agency (ANR) within the Investissements d’Avenir programme under Reference No. ANR-11-IDEX-0004-02, and more specifically within the framework of the Cluster of Excellence MATISSE led by Sorbonne Université. Financial support from the Program No. PIPOG ANR-17-CE30-000 is also acknowledged. This work was performed using HPC resources from GENCI-TGCC/CINES/IDRIS (Grant No. A0050801875). This work was also supported by EPSRC Grant No. EP/J009741/1. A.Z. was supported by a Royal Society - EPSRC Dorothy Hodgkin Research Fellowship.

APPENDIX: PARAMETERS USED IN THE AIM, PIM-FIT 1, AND PIM-FIT 2 POTENTIALS

Tables I–III list the parameters used in the AIM, PIM-Fit 1 and PIM-Fit 2 potentials, respectively.

TABLE I. Parameters used in the AIM potential for B_2O_3 , where all values are in atomic units.

A^{++}	62.630	a^{++}	3.9720	A^{--}	2227.6	a^{--}	2.6105
A^{+-}	15.798	a^{+-}	1.5465	B^{+-}	34 636	b^{+-}	4.8366
b_D^{+-}	2.1152	b_D^{--}	2.6858	c_D^{+-}	1.2479	c_D^{--}	2.5455
C_6^{--}	25.4	$C_6^{+-} = C_8^{+-}$	0.0	C_8^{--}	491.6	$C_6^{++} = C_8^{++}$	0.0
$b_6^{--} = b_8^{--}$	2.000	D	0.6981	β	1.8973	ζ	1.6230
η	7.4572	α_O	8.7893	q_B	+3	q_O	-2

TABLE II. Parameters used in the PIM-Fit 1 potential for B_2O_3 , where all values are in atomic units.

A^{+-}	23.956	a^{+-}	1.7204	A^{--}	464.06	a^{--}	2.6576
A^{++}	1015	a^{++}	6.467				
b_D^{+-}	2.372	b_D^{--}	2.955	c_D^{+-}	1.365	c_D^{--}	2.8905
C_6^{--}	25.4	$C_6^{+-} = C_8^{+-}$	0.0	C_8^{--}	491.6	$C_6^{++} = C_8^{++}$	0.0
$b_6^{--} = b_8^{--}$	1.000	α_O	6.342	q_B	+3	q_O	-2

TABLE III. Parameters used in the PIM-Fit 2 potential for B_2O_3 , where all values are in atomic units. Cations interact solely via their strongly repulsive Coulomb interaction.

A^{+-}	31.209	a^{+-}	1.8466	A^{--}	201.66	a^{--}	2.2121
b_D^{+-}	2.0564	b_D^{--}	2.975	c_D^{+-}	1.2172	c_D^{--}	3.3595
C_6^{--}	22.186	$C_6^{+-} = C_8^{+-}$	0.0	C_8^{--}	426.65	$C_6^{++} = C_8^{++}$	0.0
$b_6^{--} = b_8^{--}$	1.400	α_O	9.868	q_B	+3	q_O	-2

REFERENCES

- ¹A. C. Wright, *Phys. Chem. Glasses: Eur. J. Glass Sci. Technol. B* **59**, 65 (2018).
- ²G. E. Gurr, P. W. Montgomery, C. D. Knutson, and B. T. Gorres, *Acta Crystallogr. B* **26**, 906 (1970).
- ³C. T. Prewitt and R. D. Shannon, *Acta Crystallogr. B* **24**, 869 (1968).
- ⁴D. R. Uhlmann, J. F. Hays, and D. Turnbull, *Phys. Chem. Glasses* **8**, 1 (1967).
- ⁵G. Ferlat, T. Charpentier, A. P. Seitsonen, A. Takada, M. Lazzeri, L. Cormier, G. Calas, and F. Mauri, *Phys. Rev. Lett.* **101**, 065504 (2008).
- ⁶A. Takada, C. R. A. Catlow, and G. D. Price, *J. Phys.: Condens. Matter* **7**, 8659 (1995).
- ⁷A. Takada, C. R. A. Catlow, and G. D. Price, *Phys. Chem. Glasses* **44**, 147 (2003).
- ⁸F. Claeysens, N. L. Allan, N. C. Norman, and C. A. Russell, *Phys. Rev. B* **82**, 094119 (2010).
- ⁹G. Ferlat, A. P. Seitsonen, M. Lazzeri, and F. Mauri, *Nat. Mater.* **11**, 925 (2012).
- ¹⁰G. Ferlat, in *Molecular Dynamics Simulations of Disordered Materials: From Network Glasses to Phase-Change Memory Alloys*, Springer Series in Materials Science Vol. 215, edited by C. Massobrio, J. Du, M. Bernasconi, and P. S. Salmon (Springer, Cham, Switzerland, 2015), Chap. 14, pp. 367–414.
- ¹¹J. Nicholas, S. Sinogeikin, J. Kieffer, and J. Bass, *Phys. Rev. Lett.* **92**, 215701 (2004).
- ¹²S. K. Lee, K. Mibe, Y. Fei, G. D. Cody, and B. O. Mysen, *Phys. Rev. Lett.* **94**, 165507 (2005).
- ¹³A. Zeidler, K. Wezka, D. A. J. Whittaker, P. S. Salmon, A. Baroni, S. Klotz, H. E. Fischer, M. C. Wilding, C. L. Bull, M. G. Tucker, M. Salanne, G. Ferlat, and M. Micoulaut, *Phys. Rev. B* **90**, 024206 (2014).
- ¹⁴S. K. Lee, P. J. Eng, H.-K. Mao, Y. Meng, M. Newville, M. H. Hu, and J. Shu, *Nat. Mater.* **4**, 851 (2005).
- ¹⁵V. V. Brazhkin, Y. Katayama, K. Trachenko, O. B. Tsiok, A. G. Lyapin, E. Artacho, M. Dove, G. Ferlat, Y. Inamura, and H. Saitoh, *Phys. Rev. Lett.* **101**, 035702 (2008).
- ¹⁶P. Umari and A. Pasquarello, *Phys. Rev. Lett.* **95**, 137401 (2005).
- ¹⁷K. Trachenko, V. V. Brazhkin, G. Ferlat, M. T. Dove, and E. Artacho, *Phys. Rev. B* **78**, 172102 (2008).
- ¹⁸S. Ohmura and F. Shimojo, *Phys. Rev. B* **78**, 224206 (2008); **80**, 020202 (2009); **81**, 014208 (2010).
- ¹⁹C. Scherer, F. Schmid, M. Letz, and J. Horbach, *Comput. Mater. Sci.* **159**, 73 (2019).
- ²⁰T. F. Soules, *J. Chem. Phys.* **73**, 4032 (1980).
- ²¹M. Amini, S. K. Mitra, and R. W. Hockney, *J. Phys. C: Solid State Phys.* **14**, 3689 (1981).
- ²²Q. Xu, K. Kawamura, and T. Yokokawa, *J. Non-Cryst. Solids* **104**, 261 (1988).
- ²³W. Soppa, C. Van Der Marel, and H. W. den Hartog, *J. Non-Cryst. Solids* **101**, 101 (1988); W. Soppa and H. W. den Hartog, *ibid.* **108**, 260 (1989); W. Soppa, C. Van Der Marel, W. F. van Gunsteren, and H. W. den Hartog, *ibid.* **103**, 201 (1988).
- ²⁴H. Inoue, N. Aoki, and I. Yasui, *J. Am. Ceram. Soc.* **70**, 622 (1987).
- ²⁵A. H. Verhoef and H. W. den Hartog, *Radiat. Effects Defects Solids* **119**, 493 (1991); *J. Non-Cryst. Solids* **146**, 267 (1992); **180**, 102 (1994).
- ²⁶A. Takada, C. R. A. Catlow, and G. D. Price, *J. Phys.: Condens. Matter* **7**, 8693 (1995).
- ²⁷R. Fernández-Perea, F. J. Bermejo, and E. Enciso, *Phys. Rev. B* **53**, 6215 (1996).
- ²⁸F. J. Bermejo, J. Dawidowski, R. Fernández-Perea, and J. L. Martínez, *Phys. Rev. B* **54**, 244 (1996).
- ²⁹R. E. Youngman, J. Kieffer, J. D. Bass, and L. Duffrène, *J. Non-Cryst. Solids* **222**, 190 (1997).
- ³⁰R. Fernández-Perea, F. J. Bermejo, and M. L. Senent, *Phys. Rev. B* **54**, 6039 (1996).
- ³¹E. Kashchieva, B. Shivachev, and Y. Dimitriev, *J. Non-Cryst. Solids* **351**, 1158 (2005).
- ³²A. Takada, *Phys. Chem. Glasses: Eur. J. Glass Sci. Technol. B* **47**, 493 (2006).
- ³³M. Teter, in *Borate Glasses, Crystals and Melts*, edited by A. C. Wright, S. A. Feller, and A. C. Hannon (Society of Glass Technology, Sheffield, 1997), p. 407.
- ³⁴J. K. Maranas, Y. Chen, D. K. Stillinger, and F. H. Stillinger, *J. Chem. Phys.* **115**, 6578 (2001).
- ³⁵S. K. Fullerton and J. K. Maranas, *J. Chem. Phys.* **121**, 8562 (2004).
- ³⁶S. K. Fullerton and J. K. Maranas, *Nano Lett.* **5**, 363 (2005).
- ³⁷L. Huang and J. Kieffer, *Phys. Rev. B* **74**, 224107 (2006).
- ³⁸L. Huang, M. Durandurdu, and J. Kieffer, *J. Phys. Chem. C* **111**, 13712 (2007).
- ³⁹L. Huang, J. Nicholas, J. Kieffer, and J. Bass, *J. Phys.: Condens. Matter* **20**, 075107 (2008).
- ⁴⁰O. L. G. Alderman, G. Ferlat, A. Baroni, M. Salanne, M. Micoulaut, C. J. Benmore, A. Lin, A. Tamaloni, and J. K. R. Weber, *J. Phys. Condens. Matter* **27**, 455104 (2015).
- ⁴¹A. C. Hannon, D. I. Grimley, R. A. Hulme, A. C. Wright, and R. N. Sinclair, *J. Non-Cryst. Solids* **177**, 299 (1994).
- ⁴²R. E. Youngman, S. T. Haubrich, J. W. Zwanziger, M. T. Janicke, and B. F. Chmelka, *Science* **269**, 1416 (1995).
- ⁴³C. Joo, U. Werner-Zwanziger, and J. W. Zwanziger, *J. Non-Cryst. Solids* **271**, 265 (2000).
- ⁴⁴G. E. Walrafen, S. R. Samanta, and P. N. Krishnan, *J. Chem. Phys.* **72**, 113 (1980).
- ⁴⁵G. E. Walrafen, M. S. Hokmabadi, P. N. Krishnan, S. Guha, and R. G. Munro, *J. Chem. Phys.* **79**, 3609 (1983).
- ⁴⁶A. K. Soper, *J. Phys.: Condens. Matter* **22**, 404210 (2010).
- ⁴⁷F. Pacaud, J.-M. Delaye, T. Charpentier, L. Cormier, and M. Salanne, *J. Chem. Phys.* **147**, 161711 (2017).
- ⁴⁸M. Born and J. E. Mayer, *Z. Phys. A: Hadrons Nucl.* **75**, 1 (1932).
- ⁴⁹J. E. Mayer, *J. Chem. Phys.* **1**, 270 (1933).
- ⁵⁰M. L. Huggins and J. E. Mayer, *J. Chem. Phys.* **1**, 643 (1933).
- ⁵¹B. W. H. van Beest, G. J. Kramer, and R. A. van Santen, *Phys. Rev. Lett.* **64**, 1955 (1990).
- ⁵²A. Carré, J. Horbach, S. Ispas, and W. Kob, *Europhys. Lett.* **82**, 17001 (2008).
- ⁵³F. Pacaud and M. Micoulaut, *J. Chem. Phys.* **143**, 064502 (2015).
- ⁵⁴K. T. Tang and J. P. Toennies, *J. Chem. Phys.* **80**, 3726 (1984).
- ⁵⁵P. A. Madden and M. Wilson, *Chem. Soc. Rev.* **25**, 339 (1996).
- ⁵⁶M. Wilson, P. A. Madden, M. Hemmati, and C. A. Angell, *Phys. Rev. Lett.* **77**, 4023 (1996).
- ⁵⁷M. Wilson and P. A. Madden, *Faraday Discuss.* **106**, 339 (1997).
- ⁵⁸A. J. Rowley, P. Jemmer, M. Wilson, and P. A. Madden, *J. Chem. Phys.* **108**, 10209 (1998).
- ⁵⁹A. Aguado and P. A. Madden, *Phys. Rev. B* **70**, 245103 (2004).
- ⁶⁰S. Jahn, P. A. Madden, and M. Wilson, *Phys. Rev. B* **74**, 024112 (2006).
- ⁶¹S. Jahn and P. A. Madden, *Phys. Earth Planet. Inter.* **162**, 129 (2007).
- ⁶²P. Cieplak, F.-Y. Dupradeau, Y. Duan, and J. Wang, *J. Phys. Condens. Matter* **21**, 333102 (2009).
- ⁶³A. Aguado, L. Bernasconi, S. Jahn, and P. A. Madden, *Faraday Discuss.* **124**, 171 (2003).
- ⁶⁴B. Rotenberg, M. Salanne, C. Simon, and R. Vuilleumier, *Phys. Rev. Lett.* **104**, 138301 (2010).
- ⁶⁵M. Salanne, D. Marrocchelli, and G. W. Watson, *J. Phys. Chem. C* **116**, 18618 (2012).
- ⁶⁶J. P. Perdew, K. Burke, and M. Ernzerhof, *Phys. Rev. Lett.* **77**, 3865 (1996).
- ⁶⁷The glassy configurations used for the parameter calibration were obtained from the quench-from-the-melt technique. In consequence, the proportion of boroxol rings ($f = 22\%$) in these configurations does not match the expected experimental value ($f \approx 75\%$). However, the model contained threefold coordinated boron atoms in both boroxol ring and nonring environments, which are therefore accounted for in the parameter calibration.
- ⁶⁸P. L. Silvestrelli, *Phys. Rev. Lett.* **100**, 053002 (2008).
- ⁶⁹H. Hay, G. Ferlat, M. Casula, A. P. Seitsonen, and F. Mauri, *Phys. Rev. B* **92**, 144111 (2015).
- ⁷⁰G. Ferlat, M. Hellgren, F.-X. Coudert, H. Hay, F. Mauri, and M. Casula, *Phys. Rev. Mater.* **3**, 063603 (2019).
- ⁷¹T. Laino and J. Hutter, *J. Chem. Phys.* **129**, 074102 (2008).
- ⁷²L.-H. Kieu, J.-M. Delaye, L. Cormier, and C. Stolz, *J. Non-Cryst. Solids* **357**, 3313 (2011).

- ⁷³A. Takada, *Phys. Chem. Glasses* **45**, 156 (2004).
- ⁷⁴A. Mujica, A. Rubio, A. Muñoz, and R. J. Needs, *Rev. Mod. Phys.* **75**, 863 (2003).
- ⁷⁵U. Engberg, *Phys. Rev. B* **55**, 2824 (1997).
- ⁷⁶J. D. Mackenzie and W. F. Claussen, *J. Am. Ceram. Soc.* **44**, 79 (1961).
- ⁷⁷H. D'Amour, W. Denner, and H. Schulz, *Acta Crystallogr., Sect. B* **35**, 550 (1979).
- ⁷⁸T. Edwards, T. Endo, J. H. Walton, and S. Sen, *Science* **345**, 1027 (2014).
- ⁷⁹A. Zeidler, P. S. Salmon, and L. B. Skinner, *Proc. Natl. Acad. Sci. U. S. A.* **111**, 10045 (2014).
- ⁸⁰A. C. T. van Duin, S. Dasgupta, F. Lorant, and W. A. Goddard III, *J. Phys. Chem. A* **105**, 9396 (2001).
- ⁸¹V. V. Brazhkin, I. Farnan, K.-I. Funakoshi, M. Kanzaki, Y. Katayama, A. G. Lyapin, and H. Saitoh, *Phys. Rev. Lett.* **105**, 115701 (2010).
- ⁸²G. Carini, Jr., G. Carini, G. D'Angelo, M. Federico, and V. Romano, *J. Non-Cryst. Solids* **492**, 102 (2018).
- ⁸³M. Grimsditch, A. Polian, and A. C. Wright, *Phys. Rev. B* **54**, 152 (1996).
- ⁸⁴In the calculated structures, all B_3O_3 rings were counted as boroxol rings, irrespective of their planarity.
- ⁸⁵For boroxol rings (B_3O_3), $N_{O, \text{boroxol}} = N_{B, \text{boroxol}}$, where $N_{O, \text{boroxol}}$ and $N_{B, \text{boroxol}}$ are the numbers of oxygen and boron atoms in boroxol rings, respectively. For $g\text{-}B_2O_3$, $N_O = 1.5N_B$, where N_O and N_B are the total numbers of boron and oxygen atoms in the glass, respectively. It follows that the proportion of boron atoms in boroxol rings $f = N_{B, \text{boroxol}}/N_B = f_O N_O/N_B = f_O \times 1.5$.
- ⁸⁶The slopes obtained with the PIM-Fit 1 and AIM potentials are $-5.7 \text{ kcal (mol } B_2O_3)^{-1}$ and $-2.9 \text{ kcal (mol } B_2O_3)^{-1}$, respectively. These values convert to $-5.7/0.75 = -7.6 \text{ kcal (mol } B_2O_3 \text{ in boroxol})^{-1}$ and $-2.9/0.75 = -3.9 \text{ kcal (mol } B_2O_3 \text{ in boroxol})^{-1}$, respectively, if the glass has 75% of boron atoms in boroxol rings. Furthermore, since 1 mol of boroxol units ($B_3O_{9/2}$) is equivalent to 1.5 mol of B_2O_3 , one obtains BSE values of $-11.4 \text{ kcal (mol boroxol})^{-1}$ for PIM-Fit 1 and $-5.8 \text{ kcal (mol boroxol})^{-1}$ for AIM.
- ⁸⁷S. Pipolo, M. Salanne, G. Ferlat, S. Klotz, A. M. Saitta, and F. Pietrucci, *Phys. Rev. Lett.* **119**, 245701 (2017).